Results in Engineering 29 (2026) 108827

Contents lists available at ScienceDirect

Results in Engineering

journal homepage: www.sciencedirect.com/journal/results-in-engineering

Research paper

# Large-scale thermo-mechanical simulation of laser beam welding using high-performance computing: A qualitative reproduction of experimental results

Tommaso Bevilacqua [a], Andrey Gumenyuk [b], Niloufar Habibi [b], Philipp Hartwig [c], Axel Klawonn [a,d,*], Martin Lanser [a,d], Michael Rethmeier [e,b,f], Lisa Scheunemann [g], Jörg Schröder [c]

[a] *Department of Mathematics and Computer Science, University of Cologne, Cologne, Germany*
[b] *Bundesanstalt für Materialforschung und -prüfung (BAM), Berlin, Germany*
[c] *Institute of Mechanics, Department of Civil Engineering, University Duisburg-Essen, Duisburg, Germany*
[d] *Center for Data and Simulation Science, University of Cologne, Cologne, Germany*
[e] *Technische Universität Berlin, Berlin, Germany*
[f] *Fraunhofer Institute for Production Systems and Design Technology IPK, Berlin, Germany*
[g] *Institute of Applied Mechanics,RWTH Aachen, Aachen, Germany*

A R T I C L E I N F O

*Keywords:*
Termo-mechanical processes
Solidification cracking
High-performance computing
Domain decomposition methods
Laser beam welding

A B S T R A C T

Laser beam welding (LBW) is a non-contact joining technique that has gained significant importance in modern industrial manufacturing. One potential problem, however, is the formation of solidification cracks, which particularly affects alloys with a pronounced melting range. The aim of the present work is the development of computational methods and software tools to numerically simulate LBW. In order to obtain a sufficiently accurate solution, a large number of finite elements has to be used. Therefore, a highly parallel scalable solver framework, based on the software library PETSc, was used to solve this computationally challenging problem on a high-performance computing architecture. Finally, the experimental results and the numerical simulations are compared. They are found to be in good qualitative agreement, which confirms the validity of the numerical simulations and allows for a better interpretation of the experimentally observed strain distribution.

## 1. Introduction

Over the past decade, the laser beam welding (LBW) process has undergone significant advancements and has established itself as an efficient and economical tool in the industry. This process offers a highly concentrated energy input, minimizing thermal strain in components while enabling rapid processing with deep penetration - ideal for producing durable, high-performance parts. Key applications can be found in high-precision industries such as aerospace, energy technology, and plant and apparatus engineering. Temperature- and corrosion-resistant high-alloy steels are commonly used in these safety-critical areas. However, during welding, these materials are prone to solidification cracking - a complex phenomenon influenced by the interplay of various thermal, metallurgical, and mechanical factors [1–3]. This type of cracking typically occurs during the final stages of solidification in the mushy zone - the region where both solid and liquid phases coexist -, when tensile stresses exceed the ability of the remaining liquid to backfill gaps. Additionally, high solid fractions and an insufficient liquid flow further intensify cracking.

Therefore, an accurate determination of the ductility limits of a material and the influence of process parameters is essential for the optimization of the LBW process. This requires experimental methods to evaluate ductility in the mushy zone, that is within the brittle temperature range (BTR) [4], which spans from the solidus to the liquidus temperature. Since solidification cracking is influenced by both temperature and strain rate, precise measurement technologies are crucial along with a testing system, which is capable of applying varied strain conditions during welding. To this end, Controlled Tensile Weldability (CTW) [5], combined with high-resolution temperature and local strain measurement technologies, is an effective method, allowing, in particular, for the application of a wide range of global strains and strain rates during welding. Additionally, integrating computer-aided engineering in parallel with experimental tests provides deeper insights into the process and enhances the accuracy of ductility limit determinations, which can

* Corresponding author.
*E-mail address:* axel.klawonn@uni-koeln.de (A. Klawonn).

https://doi.org/10.1016/j.rineng.2025.108827
Received 29 October 2025; Received in revised form 12 December 2025; Accepted 19 December 2025
Available online 22 December 2025

subsequently be utilized in the design of complex manufacturing processes [6].

Here, our goal is to set up and present efficient finite element simulations of the CTW test to get new insights using highly resolved simulations, exploiting the potential of modern supercomputers. First numerical methods for the description of thermo-mechanical problems for welding were presented in [7] and [8]. thermo-mechanical welding simulations are also a topic of discussion today. In [9] the authors proposed a multiscale approach for the LBW process where the laser heat source automatically adapts to the welding regime. Here, details of the melt pool dynamics are not required, which leads to an efficient computational scheme. A calibration of thermo-mechanically Additive Manufacturing (AM) simulations in the *Simufact* [10] software for the prediction of residual stresses and distortions are presented in [11]. Moreover, a comprehensive overview of the current state of the art in numerical simulations of LBW can be found in [12]. Finite element simulations of LBW processes are typically performed in either commercial software or specialized high-performance tools, each offering distinct trade-offs. On the one hand, commercial finite element software tools like ANSYS [13,14] enable fast and flexible parametrization for model and materials and mesh refinement, but has computational limitations for large-scale coupled problems. On the other hand, specialized tools like FE2TI [15] provide high-performance capabilities, but require more effort to reproduce experimental setups accurately. To overcome these limitations, we propose a hybrid approach combining the easy-to-use commercial software ANSYS and the high-performance software FE2TI, which is based on the very efficient PETSc [16] library. The key novelty is a two-stage methodology: first, ANSYS simulates the full domain with sequential thermo-elastoplasticity, providing boundary conditions on a refined strip around the weld; then FE2TI performs fully coupled thermo-elastoplastic analysis on the region of interest at supercomputer scale. This enables high-resolution solutions within hours, which is not possible with ANSYS alone. Moreover, FE2TI's fully coupled and parallel simulations captures temperature-deformation interactions more accurately than ANSYS's sequential approach, where only the temperature field over time is computed and afterwards a temperature-driven elastoplasticity problem is solved. The coupled thermo-elastoplastic formulation is based on [17], in which finite strains were taken into account, and adapted to small strains. The plastic behavior is modeled by von Mises plasticity [18] and takes into account multilinear hardening. The computations are based on trilinear hexahedral elements for both displacement and temperature fields [19].

Despite the multitude of thermo-mechanical models of solidification processes in LBW that are available, there is no general understanding of how model parameters such as grid size, time resolution, and material parameters impact prediction accuracy and qualitatively influence strain-stress distribution results, especially in the mushy zone where solidification cracks are initiated. Furthermore, due to technical difficulties in measuring strain and stress in the solidification zone, there is a lack of experimental validation of these models, which raises reasonable doubts about their objectivity. This paper attempts to analyze phenomena in the hot cracking critical region of a resolidified weld based on a macromechanical model that takes into account the thermal and mechanical loading conditions acting on weld specimens. This model uses a data-driven formulation of the thermo-mechanical problem at a macroscopic level, which does not consider the microscopic effects of local material properties attributed to solid-phase transformation or the anisotropic effects linked to the grain structure of the weld metal. These phenomena are the subject of further studies within our collaborative project.

Overall, the goal of this work is to represent an initial qualitative comparison between experiments and numerical simulations, as well as to highlight their challenges, issues, and possible solutions. So far, we noticed qualitative similarities between these two approaches; although a quantitative comparison is not yet possible, this study still provides valuable insights. In particular, we will see how numerical simulations can be a complement to the experiments, which are limited to analyzing the surface of the plate and cannot investigate what happens inside, where crack initiation appears to take place.

**Table 1**
Chemical composition of the studied CrMnNi stainless steel (1.4301).

| Element: | C | Cr | Mn | Ni | Si | P | S | N | Fe |
|---|---|---|---|---|---|---|---|---|---|
| wt%: | 0.02 | 19.09 | 1.6 | 8.06 | 0.41 | 0.028 | $< 0.002$ | 0.095 | bal. |

Regarding the High-Performance Computing (HPC) framework in FE2TI, we use parallel domain decomposition solvers, which are designed and optimized to handle large thermo-elastoplasticity finite element problems [20,21]. More precisely, we use overlapping Schwarz domain decomposition methods (DDMs) [22] with variations of GDSW (Generalized Dryja-Smith-Widlund) coarse spaces which already showed to be robust for coupled multi-physics applications in the past; see [23–25] for details. Several additional features, such as, recycling strategies in the solver setup, adaptive time stepping, the optimal choice of sparse direct solvers, and optimized stopping criteria are exploited to further decrease the simulation time as well as the energy consumption of the simulation and to increase its computational efficiency [20].

The remainder of the article is organized as follows. In Section 2, we provide a detailed description of the experimental setup. This is followed by a description of the finite element and material models used in all computations and the exact description of the boundary value problems in ANSYS and FE2TI in Sections 3 and 4. Convergence studies, scalability results, and a comparison of the simulation data obtained from the FE2TI simulations with the experimental results are then considered in Section 5. There, also a detailed description of the solver setup of the chosen DDMs in FE2TI is given. We finish with some concluding remarks in Section 6.

## 2. Experimental setup

### 2.1. Material

For our study, we select an austenitic stainless steel sheet of AISI 304 (1.4301) grade with a thickness of 1 mm and a chemical composition as given in Table 1. Since the presence of the primary ferrite phase increases the sensitivity to hot cracking, the ferrite content is measured through metallographic analysis, the results of which indicate a ferrite content of 1.1 % for the base metal and 18 % for the fully penetrated weld seam. Generally, austenitic steels with $\delta$-ferrite content ranging from 5 % to 15 % are considered to exhibit good resistance to hot cracking during welding [26]. The sensitivity of this material to solidification cracking is therefore evaluated using the CTW test, as detailed in the following section.

### 2.2. CTW test procedure

The CTW test is a hot cracking evaluation method developed at the Bundesanstalt für Materialforschung und -prüfung (BAM) in Berlin [27]. It employs a horizontal tensile testing apparatus with a 50 kN load capacity to impose a controlled planar tensile strain perpendicular to the welding direction during welding. This method involves systematically varying the global strain rate (crosshead speed) to influence the local strain rate near the mushy zone. By evaluating crack and no-crack conditions, the test aims to determine the critical global strain and strain rate required for crack formation. In this study, as shown in Fig. 1 Left, the CTW-setup is equipped with a high-resolution sCMOS camera (see Section 2.3) and two-color infrared thermograph (see [28] for further details) to capture local deformation and temperature, respectively.

The sheet is cut into 120 mm × 500 mm specimens (Fig. 1 Right), and the manufactured notches at the center ensure the applied strain localizes in this region, that is a designed gauge area of 100 mm × 30 mm.

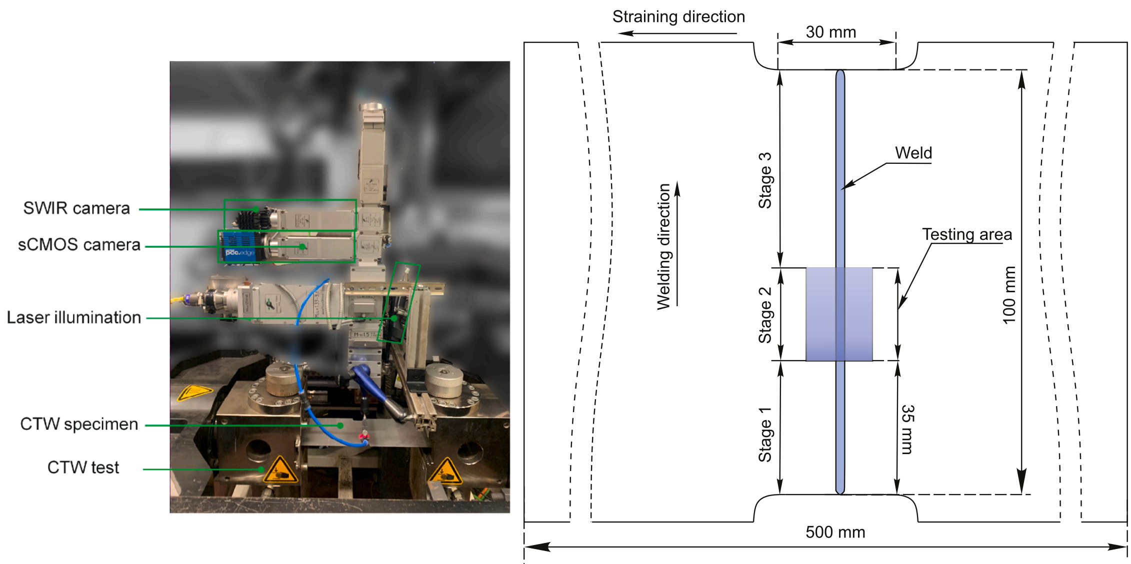


**Figure 1.** (Left) Instrumented CTW-test. (Right) Welding experiments under CTW-Test conditions-specimens arrangement.

**Table 2**
Yb:YAG disc laser characteristics and the welding parameters.

| Max. nominal power in kW | 16 | Welding speed in m/min | 1 |
|---|---|---|---|
| Wavelength in nm | 1030 | Laser power in kW | 1 |
| Fiber core diameter in μm | 200 | Ar flow rate in l/min | 20 |
| Beam parameter product (BPP) in mm × mrad | 8 | Focal position in mm | 5 |
| Focal distance in mm | 300 | Focus diameter in μm | 450 |

The test consists of three stages. In the first one, the welding process is stabilized, and a consistent temperature field is established, while no external strain is applied. The characteristics of the laser and the welding parameters are listed in Table 2.

The second stage begins after 35 mm of welding, at which point external loading is applied at a constant 6 %/s global strain. Once the maximum global strain is reached, the external loading ceases, and the welding process continues until a total weld length of 90 mm, the third stage. For this study, the maximum global strain varies from 0.02 up to 0.035 with the step size of 0.005.

### 2.3. Optical measurement technique

The welding process is recorded using a pco.edge 5.5 sCMOS camera, which is installed co-axially to the laser path; see Fig. 1 Left. To ensure a valid recording of the welding process and the re-solidified material, an external 100 W diode laser with a central wavelength of 808 nm is used for illumination. In this setup, the illuminated spot size corresponds roughly to an ellipse with dimensions of 30 mm × 60 mm. A narrow bandpass interference filter of the same wavelength and a bandwidth of 20 nm is placed in front of the camera, allowing only the wavelengths from the illumination to pass through and suppressing process emissions in all other spectral ranges during recording. The recording is conducted at 778 fps, with images stored in TIFF format at a resolution of 800 pixels × 130 pixels. The captured area covers a region of 9 mm × 1.46 mm, positioned 3.75 mm behind the weld pool along the laser beam axis, as illustrated in Fig. 7 Left.

The local straining condition is calculated at the immediate vicinity of the solidification front using a novel optical technique, based on the Optical Flow (OF) along with Lukas-Kanade (LK) algorithm [29]. Because the laser head, where the camera is inserted, typically moves while the workpieces remain stationary, only the rear part of the weld pool is evaluated. Furthermore, since solidification cracking occurs in the mushy zone, focusing on this area as the region of interest (ROI) is reasonable. This means that the ROI changes at each step, thus all the related calculations must be updated correspondingly. Therefore, the challenge in this task is tracking of the pixels in the critical temperature range to obtain the displacement, which will be used later to calculate the strain. For the ROI, an area of 430 pixels × 130 pixels (4.8 mm × 1.46 mm) is considered.

The ROI can be imagined as a mass balance for the steady-flow process that has one inlet and one outlet. The material pixels, during solidification, will enter the evaluation region from the inlet boundary and be tracked until they exit from the opposite boundary or the outlet. The new pixels, which exceed the edge of the ROI due to the movement of the material, take the displacement values of 0; then, they can be considered in the displacement computation. After estimating the displacement between two sequential frames, the main displacement field can be warped according to the newly computed displacement and then added to the temporary displacement field. The current algorithm is updated to provide a more robust computation of displacements by means of OF algorithms accounting for averaging over several frames. Based on the estimated displacements, the Green-Lagrangian strain can be computed for each frame.

## 3. Finite element modeling

### 3.1. Material model in ANSYS

In ANSYS, the material behavior is modeled using a multilinear isotropic hardening plasticity model based on the von Mises yield criterion (see Fig. 3 Bottom). Initially, the material exhibits linear elastic behavior, defined by a temperature-dependent Young modulus and Poisson ratio. Upon reaching the yield point, the material transitions into plastic deformation, described by piecewise linear hardening curves for each temperature. This approach captures the nonlinear stress-strain response and accounts for the material's strength degradation at elevated temperatures, making it suitable for simulating ductile materials under complex loading and thermal conditions.

### 3.2. Fully coupled thermo-elastoplasticity at small strains (FE2TI)

To perform the large finite element simulations carried out on our FE2TI library, we equipped it with an efficient and lightweight software interface in order to take the phenomenological material models implemented in the finite element library FEAP [30]. This allows to combine the flexibility of FEAP in defining complex material models and our highly scalable, PETSc-based solver framework.

More precisely, for the simulation of LBW processes and the CTW tests in FE2TI, a material model was implemented in FEAP that mimics the thermo-elastoplastic material behavior, see [17], at small strains. Additionally, a hexahedral finite element with $\bar{\boldsymbol{B}}$-formulation, see [19], was added. For the thermo-elastoplastic model, an additive decomposition of the total strains into an elastic part $\varepsilon^e$, a plastic part $\varepsilon^p$, and a thermal part $\varepsilon^t$ is assumed, such that $\varepsilon = \varepsilon^e + \varepsilon^p + \varepsilon^t$. Thus, the applied free energy function $\psi$ can be formulated, which is dependent on the thermo-elastic strains $\varepsilon^{te} = \varepsilon^e + \varepsilon^t$, the temperature $\theta$, and the strain-like internal variable $\alpha$, i.e.

$$\psi\left(\varepsilon^{te}, \theta, \alpha\right) = \frac{1}{2}\kappa\left(\mathrm{tr}\varepsilon^{\mathrm{te}}\right)^2 + \mu\|\mathrm{dev}\varepsilon^{\mathrm{te}}\|^2 - \mathrm{c}_\rho\left(\theta\ln\frac{\theta}{\theta_0} - \theta + \theta_0\right) - 3\alpha_T\kappa\left(\theta - \theta_0\right)\mathrm{tr}\left(\varepsilon^{\mathrm{te}}\right) + \mathrm{f}(\alpha) \tag{1}$$

comp[17]. Here, $\kappa$ denotes the bulk modulus, $\mu$ is the shear modulus, $c_\rho$ is the heat capacity, $\theta_0$ is the initial temperature, $\alpha_T$ is the heat expansion coefficient, and $f$ is the hardening function. In addition to the free energy function the balance of momentum

$$\mathrm{div}\boldsymbol{\sigma} + \boldsymbol{f} = \boldsymbol{0} \text{ with } \boldsymbol{\sigma} = \boldsymbol{\sigma}^T \tag{2}$$

and the balance of energy

$$\rho r - \div \boldsymbol{q} + \rho\theta\frac{\partial^2\psi}{\partial\theta\partial\varepsilon} : \dot{\varepsilon} + \rho\theta\frac{\partial^2\psi}{\partial\theta^2}\dot{\theta} = 0 \tag{3}$$

need to be considered. In this case, $\boldsymbol{f}$ describes the body forces and $\boldsymbol{q}$ describes the heat flux vector. The application of the entropy inequality results in the constitutive equations $\boldsymbol{\sigma} = \partial\varepsilon^{te}\psi$, which describes the relationship between stresses and strains, and $\beta = \partial\alpha\psi$, which describes the relationship between the strain-like internal variable $\alpha$ and the stress-like variable $\beta$. To describe the plastic behavior, a von Mises yield criterion

$$\Phi = \|\mathrm{dev}\boldsymbol{\sigma}\| - \sqrt{\frac{2}{3}}\left(\mathrm{y}_0 + \beta\right), \tag{4}$$

see [31], is applied where $y_0$ denotes the yield strength, which is a function of the temperature and the accumulated plastic strains. By the approximation of the complex inelastic material behavior with the von Mises plasticity we neglect microstructural effects and the evolution of anisotropy. On a phenomenological, macroscopic level, this also appears to be feasible in view of the available experimental data.

The partial differential equations (PDEs) are time-dependent and nonlinear. We use an implicit Euler scheme to discretize the nonlinear system in time and Newton's method to linearize it in each time step. Let us remark that the resulting coupled linear systems have a two-by-two block structure where the first diagonal block represents the mechanical problem and the second one the thermal diffusive problem. The coupling is nonlinear and not symmetric. Besides usual boundary conditions of Dirichlet- and Neumann-type for displacements and temperature, we have to implement the heat entry of the laser in the system, which is described in the following section.

### 3.3. Heat source modeling

The action of the laser is modeled as a constraint on a volume over the temperature field, that represents the molten region of the metal (melting pool); see Fig. 2c. To achieve this, we utilize a surface model derived from experimental data to represent this region and we move this geometry along the welding direction during the time iterations at a velocity of $1.0\,\mathrm{m/min}$, see Table 2. This model, also known as Equivalent Heat Source (EHS), is based on the approximation of the isotherms of the melt pool using Lamé curves; see [32,33].The initial temperature of the metal is set uniformly to $\theta_0 = 20°\mathrm{C}$ and the temperature within the melting pool is set to the liquidus temperature of the material of $\theta_{\mathrm{liq}} = 1460°\mathrm{C}$. While ANSYS allows the initial temperature degrees of freedom (DOFs) to be instantly set to $\theta_{\mathrm{liq}}$, in the FE2TI framework, this must be enforced through a linear increment for stability reasons. A heating procedure (initialization phase) is therefore implemented to ensure that the temperature $\theta_{\mathrm{liq}}$ is reached within the melting pool after $0.1\ s$. After

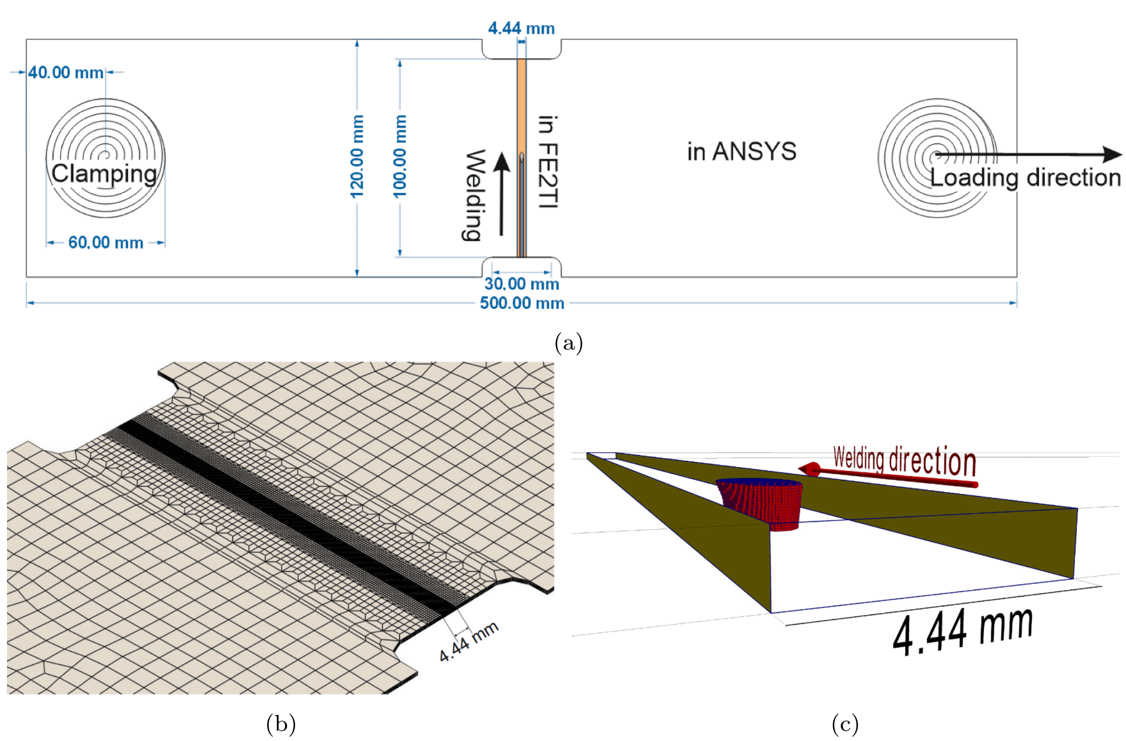


**Figure 2.** (a) Schematic illustration of CTW test; the whole specimen was used for the ANSYS simulations, while the FE2TI simulations focus on the middle strip. (b) The mesh pattern used in the ANSYS simulation. (c) Zoom to the FE2TI simulation sub-geometry. In yellow the surfaces where the boundary conditions from ANSYS are applied, in red the discrete representation of the melting pool using hexahedral finite elements. (For interpretation of the references to colour in this figure legend, the reader is referred to the web version of this article.)

this initialization phase, the movement of the melting pool starts and it is necessary to constantly update the temperature constraints, since in each time step some finite elements enter the melting pool and some leave it. In contrast to the initialization phase, when a temperature DOFs enters into the moving melting pool is immediately set to $\theta_{\text{liq}}$, which caused no problems in the simulations so far.

## 4. Boundary value problem and material parameter

### 4.1. Boundary value problem

The boundary value problem at hand, which is solved in the simulations, is based on the experimental setup of the CTW test. In the ANSYS simulations the entire system is used, while a section of the specimen is considered for the simulation with FE2TI. The entire specimen therefore has dimensions of 500 mm by 120 mm and a thickness of 1 mm. In the center of the system there is a cut-out over a length of 30 mm, which is tapered by 10 mm on both sides to 100 mm. This is intended to concentrate the arising strains in the area of the cut-out; see Fig. 2a.

For the simulation in ANSYS, a thermal analysis is first performed to determine the temperature history. Then, the temperature results are applied incrementally to the mechanical model to calculate stresses and strains. A step size of 0.001 s is defined for both processes. The system is meshed using 88 780 elements with a finer size of $0.185\,\text{mm} \times 0.185\,\text{mm} \times 0.2\,\text{mm}$ at the critical region. The resulting finite element mesh is shown in Fig. 2b. For this regard, the element types of SOLID70 (3-D Thermal Solid) and SOLID186 (3-D 20-Node Structural Solid) for the thermal and mechanical analyses are used, respectively.

To simplify the computation, the laser itself is not simulated, but the heat source model described in Section 3.3 is used. More precisely, we recall that the isotherm of the liquidus temperature (1460°C) is predefined and moved forward along the welding direction identically to the real welding process. A constant temperature therefore prevails within the isotherm, while the temperature outside the isotherm is freely adjustable. The mechanical boundary conditions are identical to those of the experiment. For this purpose, two circular areas with a diameter of 60 mm are defined at opposite ends in which the boundary conditions are applied. The two areas are centered along the welding direction and have a distance between center and the outer edge of the specimen of 40 mm. In one area, all displacements are prevented so that a clamping is present, while in the second area the displacements in the $x$- and $z$-directions are prevented and a prescribed displacement is applied for the $y$-direction. For the applied displacements, a maximum strain of 2.5 % with a strain rate of 6 %/s is assumed. However, the strains are not applied right from the start, but increase with the strain rate from the point at which the laser has traveled a distance of 35 mm. Once the maximum strains have been reached, they are not increased any further but remain constant until the end of the welding process. This mimics the behavior of the experiment as described in Section 2.2.

As already mentioned, the simulation in FE2TI is carried out on a sub-geometry of the simulation with ANSYS which results in a cuboid with a length of 100 mm, a width of 4.44 mm and a height of 1 mm; see Fig. 2a. Trilinear structured hexahedral elements are used to create a highly resolved mesh with up to 4.4 millions of elements. As the simulation with FE2TI only solves a subproblem, the mechanical and thermal boundary conditions are extracted from the simulation with ANSYS at the corresponding edges of the associated sub-geometry. These boundary conditions are then applied as Dirichlet boundary conditions on the lateral surfaces along the welding direction (see Fig. 2c).

More precisely, on these lateral faces we export the nodal values from ANSYS at each time step. Since the ANSYS mesh is structured and uniform in the strip region, the two lateral faces of the FE2TI subdomain coincide with element faces, avoiding geometric projection errors. The data transfer is minimal because only the boundary nodal values are exported rather than the full ANSYS solution. In FE2TI, the ANSYS data are used to reconstruct Dirichlet boundary values at the finer FE2TI mesh nodes: for each boundary node, the surrounding ANSYS nodes are selected and values are obtained by a bilinear interpolation in space and linear interpolation in time. Where FE2TI nodes coincide with ANSYS nodes, values are imposed exactly. Since the mapping operates directly on the nodal ANSYS solution using only standard interpolation, the boundary conditions in FE2TI reproduce the ANSYS interface solution up to the interpolation error inherent to the ANSYS discretization. Finally, the thermal constraints to represent the laser action are enforced as previously described in Section 3.3.

### 4.2. Material parameters

The temperature-dependent material parameters are determined using the *Sysweld* [34] software and made available for simulation in the form of tabular values. Here, piecewise linear interpolation is performed between the given data and the support points $\theta_k < \theta \le \theta_{k+1}$. We obtain

$$\theta_k < \theta \le \theta_{k+1} \;\Rightarrow\; p = p_k + \frac{p_{k+1} - p_k}{\theta_{k+1} - \theta_k} \cdot \left(\theta - \theta_k\right) \text{ with } p \in \{E, \nu, \alpha_{\text{T}}, c_\rho, \lambda\}, \tag{5}$$

where $\theta_k$ and $\theta_{k+1}$ reflect the temperatures of a respective data point and $\theta$ the intermediate temperature at which the material parameters are evaluated. Accordingly, $p$ stands for the material parameter to be determined and $p_k$ and $p_{k+1}$ for the material parameters of the associated temperatures. Additionally, the latent heat effects are approximated by the heat capacity profile, which increases sharply in the range between 1427°C and 1500°C. This requires a sufficiently fine temperature resolution in this range. Despite the data-driven implementation of material parameters, it is possible to describe the heat capacity analytically from [35] and [36]. However, from the engineering point of view this leads to very similar results.

For the simulation the Young modulus $E$, the Poisson ratio $\nu$, the coefficient of thermal expansion $\alpha_T$, the specific heat capacity $c_\rho$, the thermal conductivity $\lambda$ and the density $\rho$ are required. All these values, except for the density, are evaluated for a temperature range from 0°C to 2000°C and are shown in Fig. 3 Top.

Due to the fact that no density data is available in *Sysweld*, a density of $7919\,\text{kg/m}^3$ was taken from [37] and it is assumed to be constant over temperature.

Since a thermo-elastoplastic material behavior is assumed, values for the yield stress $y_0$ and the linear hardening parameter $h$ are needed. Both values depend on two variables, the temperature $\theta$ and the accumulated plastic strains $\alpha$. The available yield curves are shown in Fig. 3 Bottom. As a result of the dependency on two variables, a two-step interpolation scheme is necessary. If the value of the yield stress and the linear strain hardening parameter has to be evaluated for a temperature $\theta_n$ and an accumulated plastic strain $\alpha_n$, the first step is to interpolate with respect to the temperature. Thus, $\theta_l < \theta_n < \theta_{l+1}$ applies and interpolation takes place at the points $\alpha_k$ and $\alpha_{k+1}$. It holds that

$$\begin{aligned} y(\alpha_k, \theta_n) &= y_0(\alpha_k, \theta_l) + \frac{y_0(\alpha_k, \theta_{l+1}) - y_0(\alpha_k, \theta_l)}{\theta_{l+1} - \theta_l}\left(\theta_n - \theta_l\right) \\ y(\alpha_{k+1}, \theta_n) &= y_0(\alpha_{k+1}, \theta_l) + \frac{y_0(\alpha_{k+1}, \theta_{l+1}) - y_0(\alpha_{k+1}, \theta_l)}{\theta_{l+1} - \theta_l}\left(\theta_n - \theta_l\right). \end{aligned} \tag{6}$$

In a second step, the values of Eq. (6) are used and an interpolation is carried out with respect to the accumulated plastic strains. Now, $\alpha_k < \alpha_n < \alpha_{k+1}$ applies and the following holds for the interpolation

$$y(\alpha_n, \theta_n) = y(\alpha_k, \theta_n) + \underbrace{\frac{y(\alpha_{k+1}, \theta_n) - y(\alpha_k, \theta_n)}{\alpha_{k+1} - \alpha_k}}_{=h}\left(\alpha_n - \alpha_k\right). \tag{7}$$

In addition to determining the yield stress $y(\alpha_n, \theta_n)$, the hardening parameter $h$, which reflects the quotient of yield stress and accumulated plastic strains, is computed simultaneously.

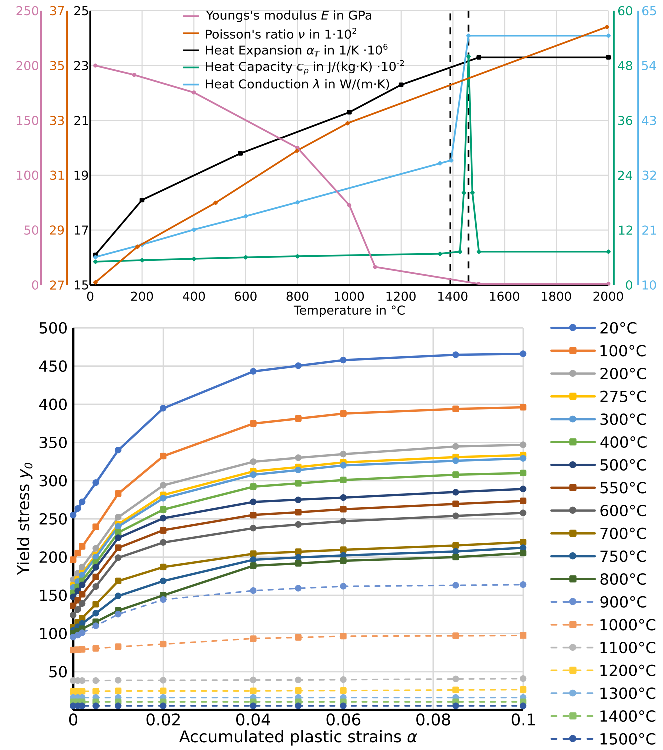


**Figure 3.** (Top) Material parameters for the used austenitic chrome-nickel steel 1.4301. The data originate from the software *Sysweld* [34]. The first dashed vertical line visualizes the solidus temperature $\theta_{\mathrm{sol}} = 1390°\mathrm{C}$ and the second dashed line visualizes the liquidus temperature $\theta_{\mathrm{liq}} = 1460°\mathrm{C}$. (Bottom) Yield curves for the used austenitic chrome-nickel steel 1.4301. The data originate from the software *Sysweld*.

## 5. Parallel high resolution simulations on modern high-performance computers

As described above, discretization in space using finite elements, discretization in time, and using Newton's method to linearize the nonlinear thermo-elastoplastic problem, results in a sparse linear system in each Newton iteration. Caused by the high resolution of our finite element meshes, we have millions of DOFs in our computations and thus the solution of extremely large linear systems has to be parallelized using HPC resources. In general, iterative solvers combined with efficient preconditioners are well-suited for this purpose. This motivates our choice of the Generalized Minimal Residual (GMRES) method in combination with suitable domain decomposition preconditioners.

DDMs are powerful techniques used to solve PDEs and the parallelization is based on a divide-and-conquer paradigm. Therefore the computational domain is decomposed into smaller subdomains, the PDEs are then localized to the subdomains, and the resulting subdomain problems are solved independently and coupled in an iterative process; see Fig. 5 Top. Among all overlapping DDMs, the additive Schwarz preconditioner is a popular choice, where information is exchanged within the overlap of neighboring subdomains in each GMRES iteration, that is, in each application of the Schwarz preconditioner. For robustness and scalability, a second level of correction, often referred to as a coarse space, is introduced. This coarse space facilitates the exchange of global information improving the overall convergence by addressing long-range dependencies and ensuring efficient scaling with the number of subdomains. Specifically, in our work, we make use of a two-level Schwarz method with Generalized Dryja-Smith-Widlund (GDSW) coarse spaces to enhance the efficiency and scalability of the domain decomposition approach; see [23,24] for details. Let us note that GDSW coarse spaces have some important advantages which make them a perfect choice in LBW simulations. They can be used with general subdomain shapes, computed algebraically using only information from the system matrix, and are applicable to multi-physics problems, as, for example, thermo-elastoplasticity problems, in a monolithic fashion [20].

The aforementioned Schwarz preconditioners are implemented in the software package FE2TI, a C/C++ library with an MPI/OpenMP [38] hybrid parallel implementation exploiting the PETSc library. The FE2TI software has already been shown to scale efficiently to more than one million parallel ranks solving realistic deformation scenarios of dual-phase steels; see [15,39] for details. Moreover, as already mentioned, we equipped it with an interface to the FEAP library [30], to exploit the finite elements and material models from FEAP. Finally, the local and coarse problems in the Schwarz preconditioners are solved exactly using the version of PARDISO implemented in the Math Kernel Library [40,41].

All of these features are used to model the CTW test on a portion of the plate. Specifically, we analyze a strip with dimensions 4.44 mm in width, utilizing highly resolved meshes consisting of millions of DOFs, distributed across thousands of parallel compute cores. We simulate 2.4 s of the CTW test, subdivided as follows: from 0 s to 0.1 s the heat-up procedure is performed, keeping the laser fixed at its initial position; from 0.1 s to 1.9 s the laser moves at a velocity of 1 m/s (Stage 1 in Section 2.2); finally from 1.9 s to 2.4 s, the laser continues to move while an external strain is applied (Stage 2 in Section 2.2).

Throughout the simulation, boundary conditions on the side faces of the strip are interpolated from the ANSYS simulation of the whole plate, while the laser action is modeled as described in Section 3.3. A time step size of $\Delta t = 0.001$ s is always used (except when explicitly stated), resulting in a total of 2 400 iterations. In each time step, Newton's method is applied until the global residual falls below an absolute tolerance of $10^{-3}$. For the linear systems, the GMRES method is employed, which is restarted every 100 iterations, with a stopping criterion of either a relative residual of $10^{-6}$ or an absolute residual of $10^{-10}$ based on the unpreconditioned norm.

### 5.1. Convergence study

To choose suitable discretization grid sizes in space and time, we perform a convergence study on the complete CTW simulation. We analyze the strip with a width of 4.44 mm, utilizing different, highly-resolved meshes, consisting of 324 600, 2 330 636, 7 573 312 and 17 607 828 DOFs distributed across 360, 720, 1440 and again 1440 cores respectively.

Even if, for the moment, our final goal is to only achieve a qualitative comparisons with the experimental results, a grid convergence study is needed to test our FEM implementation. To this end, we focus our analysis on measuring three quantities of interest located on the surface of the plate regarding the $y$-strain, namely the mean value evaluated within the ROI as well as the maximum and mean value evaluated on a small green window (GW) as shown in Fig. 4a. Additionally, since these quantities are computed exclusively on the plate's surface, we also consider the maximum strain value within the ROI, extending the analysis along the vertical direction, where we expect to observe higher values. Since we do not perform a quantitative comparison between numerical and experimental results, in all these numerical simulations, the ROI size corresponds to the entire Field of view (FOV).

In Fig. 4b, we report these quantities calculate over the time iterations. From these results, we observe that mesh convergence is achieved only up to 2.1 s, which corresponds to the time after 0.2 s of the application of the external strain. After this time, the plastic effect becomes stronger and the solution seems to be strongly mesh-dependent.

This mesh-dependent material behavior is typical for a stress-strain relation with softening. Based on empirical evidence, we suspect the loss of rank-1 convexity at selected locations; this is also supported by the images of plastic strains in Fig. 8, which correspond to typical localization bands. Due to the complex thermo-mechanically coupled material behavior and the temperature-dependent material parameters, a more

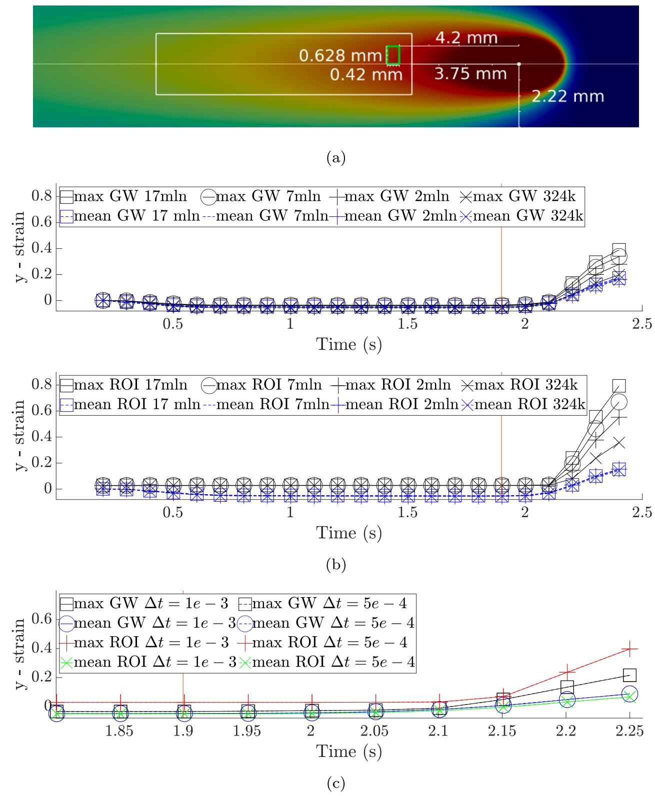


**Figure 4.** (a) Position of the ROI and the small green region over the temperature field. (b) Plot of the quantities of interest over the time steps for the meshes with 324 600, 2 330 636, 7 573 312 and 17 607 828 DOFs. (c) Plot of the quantities of interest for the meshes with 17 607 828 DOFs, with time steps 0.001 s and 0.0005 s. (For interpretation of the references to colour in this figure legend, the reader is referred to the web version of this article.)

in-depth analysis is required here in the future. To overcome this possibly pathological behavior, existing nonlocal continuum formulations in integral and differential form could be used. The latter, also referred to as gradient-enriched continua, have been successfully applied in the fields of elasticity, plasticity, and damage and provide a robust framework for the analysis of size effects. However, these formulations generally require higher derivatives of certain field functions. Since the qualitative behavior does not change for a finer mesh and in order to save computational resources, for our numerical simulation we use the finer mesh with 17 607 828 DOFs, corresponding to an element size of about 0.05 *mm* for the scalability test, and a mesh with 7 573 312 DOFs for the results in Section 5.3.

To determine the appropriate time step size for the temporal discretization, we conduct a small convergence study. Using the restart option implemented in FE2TI, we simulate the process over the time interval from 1.8 s to 2.25 s during which the plastic effects are most pronounced. The study employs the finer mesh with 17 607 828 DOFs, and the time step size is halved to $\Delta t = 0.0005$ s. The results of this analysis, presented in Fig. 4c, show that the convergence in time is reached and a time step of $\Delta t = 0.001$ s is sufficient and therefore used in all following computations.

### 5.2. Scalability result

To prove the efficiency of our parallel software for the explicit application of LBW we perform a parallel strong scaling test. Therefore, we choose a setup with a fixed mesh resolution and measure the acceleration regarding the time to solution when increasing the number of computational cores. More precisely, we use a setup close to a production run, that is, we fix the total problem size to 17 607 828 million DOFs while scaling up the resources. In Fig. 5 Bottom, we report the average computing times required to assemble the problem, build the preconditioner, and solve the linear systems.

In this strong scaling test, and in all the other numerical simulations in this work, we are using a two-level additive Schwarz preconditioner with an overlap of one layer of finite elements and a GDSW-RGDSW coarse space designed for a thermo-elastoplasticity problem; see [20] for more details. To enhance the efficiency of our solver, we employ a recycling strategy and the preconditioner is only set up once in each time step; see [20] for details.

The results generally indicate a good scaling behavior and the runtime decreases as additional cores are utilized. While scalability is nearly perfect up to 720 cores, we observed less improvement when scaling from 720 to 1 440 cores and a further deterioration from 1 440 to 2 880. Regarding the preconditioner timings, this is primarily due to the direct solver required to handle the coarse space, which becomes large at this scale while, at the same time, the local subdomain problems become smaller and smaller. Let us note that for a larger problem with more than 17 million DOFs also more than 1 440 cores can be used efficiently. All in all, we are able to reduce the average time for one time step from 313.3 s on 90 cores to 21.0 s exploiting 1 440 cores, which corresponds to an excellent parallel efficiency of 93 %. Due to the motivations explained before, we note that the parallel efficiency drops to 64 % when computed on 2 880 cores. Therefore, for this specific problem setup, the range between 720 and 1 440 cores seems to be optimal.

### 5.3. Numerical simulation of CTW test and comparison with real experiment

In order to compare our numerical simulations with the physical experiments, we utilize a high-resolution mesh consisting of 7 573 312 DOFs, distributed across 1440 cores. Again, we simulate 2.4 s of the CTW test, with a time step size of $\Delta t = 0.001$ s. We report that the complete simulation requires, on average, approximately 49 GMRES iterations for each linear system with 8 Newton iterations in each time step. The total time for the simulation is 72 222 s that corresponds to an excellent 30.1 s per time step. Let us note that we chose the parameters, especially the time step size, the mesh resolution, the number of cores, and the preconditioner setup, based on the convergence tests and scalability tests documented in Sections 5.1 and 5.2.

In Fig. 6, we show the distribution of different strain evaluations, at the time points $t = 2.0$ s (left column) and $t = 2.2$ s (right column), computed during the complete simulation. From top to bottom, the first two rows report the total strains in the $x$- and $y$-direction, that is the strains in the welding and its orthogonal direction, respectively, while the third and fourth rows depict the same quantities computed by using an approach similar to the optimal framework technique. This means that in the two last rows, we only depict the fluctuations after a point is covered by a moving region. This area, that includes the ROI, is placed 3.75 mm behind the welding seam, and a reinitialization of the displacements to the current value takes place.

The results show that higher values for the total strains in the $x$-direction occur in the area of the melt pool. This correlates with the high temperatures and the tendency of the material to expand. Outside the melt pool, little to no strains appear while slight tensile strains develop in front of the melt pool (Fig. 6g,h). For the strains in the $y$-direction, the data indicates that compressive strains initially form in and behind the weld pool, while the surrounding area exhibits little to no strain (Fig. 6e). Over time and with increasing external load, the distribution changes, and the applied tensile strains affect the region directly behind the melt pool. Two strips of tensile strains become visible (Fig. 6f). For the fluctuations of the strains in $x$-direction, the deviations range between one fifth and one third of the total strains. However, increased pressure zones develop in the area behind the melt pool due to the cooling that has already begun and the further heating of the area in front (Fig. 6c,d). The fluctuations in $y$-direction reach the same order

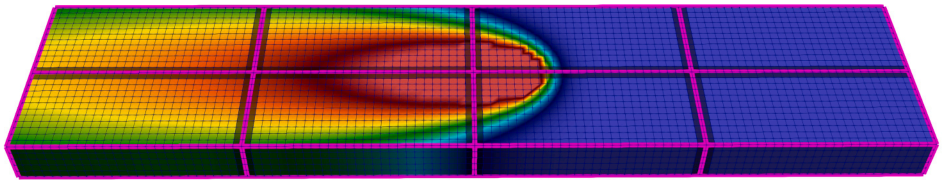

| $Cores$ | $Coarse$ | $T_{PC}$ | $T_{GMRES}$ | $T_{Ass}$ | $T_{Tot}$ |
|---|---|---|---|---|---|
| 90 | 1062 | 234.8 | 37.0 | 33.0 | 313.6 |
| 180 | 2142 | 104.2 | 24.4 | 17.0 | 150.6 |
| 360 | 5358 | 51.6 | 12.2 | 9.2 | 82.0 |
| 720 | 11783 | 18.4 | 6.9 | 5.2 | 33.4 |
| 1440 | 23656 | 10.0 | 4.8 | 3.8 | 21.0 |
| 2880 | 49468 | 6.04 | 6.36 | 1.9 | 15.2 |

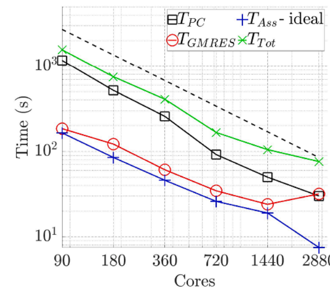


**Figure 5.** (Top) Example of an overlapping domain decomposition of a portion of the thin metal plate into overlapping subdomains. The overlap is visible as the opaque region, while the non-overlapping domain decomposition is highlighted in magenta. Each subdomain is associated to a single MPI rank. (Bottom) Strong scalability test for the first 0.005 s of a LBW process simulation with $\Delta t = 0.001$ s and 17 607 828 million DOFs. On the left, the table reports the average timings per time iteration, where $Cores$ represents the number of MPI ranks, $Coarse$ is the size of the coarse space, $T_{PC}$ is the time to construct the preconditioner, $T_{GMRES}$ is the time to compute the solution, $T_{Ass}$ is the time to assemble the FEM matrices and $T_{Tot}$ is the total time per iteration. On the right, the logarithmic plot shows the cumulative timings over the LBW simulation.

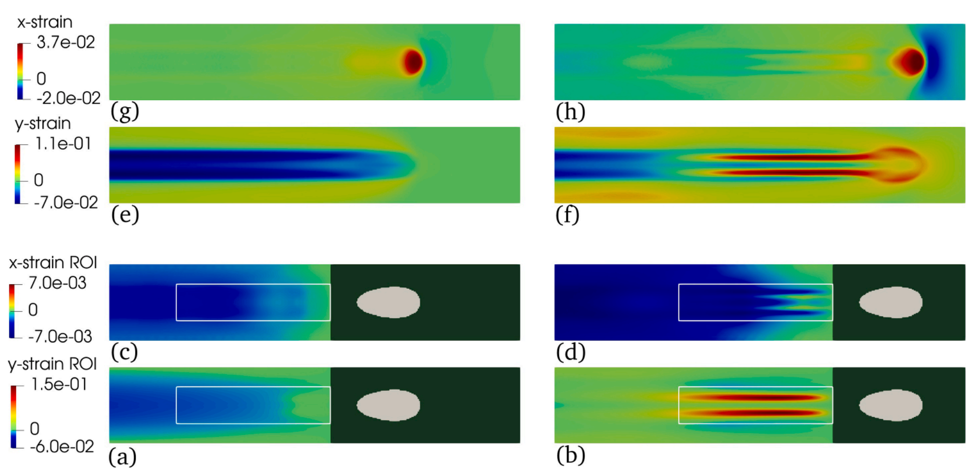


**Figure 6.** Strain distribution on the surface of a fixed section of the plate from 24 to 44 mm. From top to bottom: the $x$-strain, $y$-strain, and again the $x$- and $y$-strain with the optical framework technique. The white rectangle shows the position of the ROI with respect to the melting pool. On the left columns the distribution of these values is represented at 2.0 s, while on the right one at 2.2 s.

of magnitude as the total strains (Fig. 6a,b). The external load likely plays a primary role in this behavior. The two strips of tensile strains at time $t = 2.2$ s also appear (Fig. 6b). The absolute values compared to the total strains increase for the tensile range. This results from the fact that before entering the ROI, a compression range existed, which has now shifted to a tensile range. As a result, the difference between the values can exceed the absolute value.

Fig. 7 Right shows the experimental results in comparison to the numerical results. The diagram illustrates the $y$-strain shortly before (frame 902) and shortly after (frame 1100) the start of the application of the external load. The frame rate of the recordings corresponds to 778 fps, see Section 2.3. Thus, one frame equals approximately $1.285 * 10^{-3}$ seconds, while frame 1000 corresponds approximately to the time of load application. Although the absolute values of the strains are not identical to the numerical results, the strip-shaped profile of a tension band behind the melt pool on the outer area of the previously melted area can also be seen here directly after the application of the external load. The reasons for the differences in the absolute values of the strains can be manifold. On the one hand, the optical framework technique employs a relatively coarse meshing, which, in comparison to the highly refined FEM mesh, may lead to less precise results. Furthermore, in an experimental setting, no simplifications can be made, whereas the numerical simulation only considers a thermo-elastoplastic material behavior on the macroscale, while the model completely disregards microstructural processes occurring during cooling.

Fig. 8 depicts the cross-section at a distance of 35 mm from the edge where the welding process began, shown for the time points $t = 2.1$ s and $t = 2.2$ s. The figure presents the temperature, the strains in $y$-direction, and the equivalent plastic strains. The temperature field exhibits a uniformly distributed temperature within the solidifying material for both time points. However, in the strain distribution, a cross-shaped pattern emerges, becoming more visible as time progresses. This cross-shaped distribution indicates localization bands. This means that the strains increase significantly and become localized. The underlying cause is typically the interaction between thermal and mechanical effects; see [42].

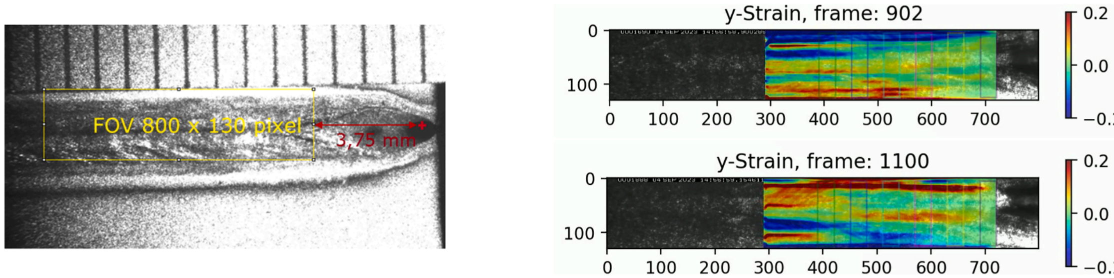


**Figure 7.** (Left) FOV of the camera image. (Right, scale is in mm) Distribution of the $y$-strain shortly before (frame 902) and shortly after (frame 1100) the external load application in the observed ROI, scale of both x and y axis is in pixel.

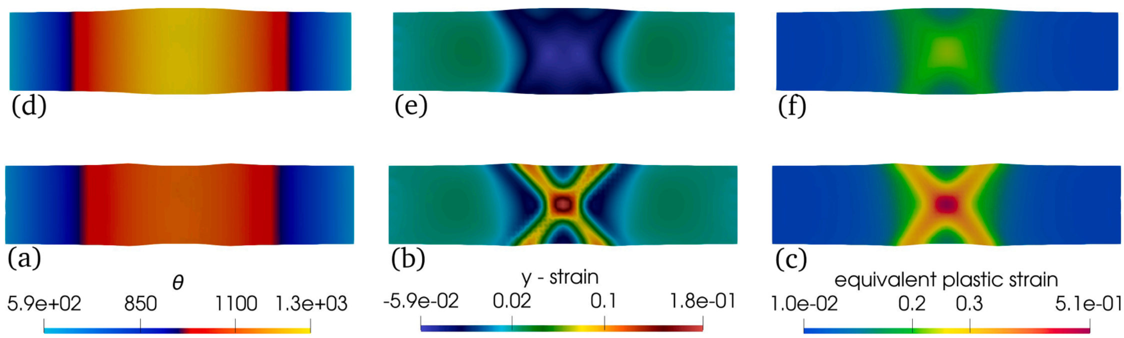


**Figure 8.** From left to right: temperature $\theta$, $y$-strain and equivalent plastic strain of a cross section of the plate positioned 35 mm from the edge. The slices are taken at two different time steps, namely 2.1 s and 2.2 s.

Based on the localization, we can conclude that the cracks observed in the experiment originate from inside the workpiece and later propagate to the surface. This aspect can not be identified by the optical frame technique, since this approach only detects changes at the surface and is therefore unable to capture cracks that emerge from within the material. In general, it can be said that the qualitative comparison between experiment and simulation already provides information or an indication of the possible formation of hot cracks. The consistency of the deformation behavior on the surface of the workpiece indicates that the simulation can provide valuable additions to the experimental data. The insight into the interior of the sample shows the shear bands typical for metals. These are a key factor for failure. It should be added that the use of the HPC environment is essential due to its extremely fine resolution of the relevant area around the molten pool.

### 5.4. Limitations and potential error sources

The results show that qualitative agreement between experiments and simulations can be achieved. However, quantitative agreement was not achieved, which may result from the simplifications in the simulations. This subsection briefly explains which simplifications were made and their potential impact. One important aspect here is the evaluation of the results. An extensive convergence study was carried out for the numerical results, see Section 5.1, for which convergence is observed until strong plastic effects occur. After this, mesh dependency increases due to strain localization. On the other hand, the applied experimental technique has also its limitations in strain estimation. Because of used algorithm for displacement calculation based on the points tracking as described in Section 2.3, computational errors accumulates for the regions located to the left side of the ROI and the resulting accuracy of calculated strain is reduced from its right to left side which complicate direct interpretation of the experimental results and quantitative comparison to the numerical one. Nevertheless, we have observed qualitatively similar behavior in strain distribution (i.e. strain localization aside the crack initiation region) as obtained in the simulation.

## 6. Conclusions

In the present work, large-scale thermo-mechanical simulations of LBW processes, more precisely simulations of the CTW test, were conducted using highly resolving discretizations and high-performance computing to obtain high-fidelity numerical results. The chosen hybrid approach combining the strengths of the commercial software ANSYS and the high-performance computing framework FE2TI resulted in detailed virtual insights into the welding process. Especially the divide-and-conquer parallelization paradigm used in FE2TI enabled large-scale simulations exploiting modern supercomputers and led to a very fine resolution of the surrounding of the weld seam.

The dimensions of the geometry, boundary conditions, and external loading conditions of the boundary value problem are taken from the experimental setup. The material parameters required for the simulation were computed using the *Sysweld* simulation software based on the chemical composition of the material; see Table 1. The outcome is that the numerical results are in good qualitative agreement with the experimental ones, particularly with respect to strain distribution and localization phenomena, despite the complexity of the thermo-mechanical coupling in LBW. However, the quantitative agreement is still limited, which may be due to various factors, such as not considering the dendritic microstructure in the simulation, the coarse meshing of the optical framework in the experiment, or the omission of physical processes in the melt pool as phase-transformation effects. Furthermore, to fully trust the FE simulation, the results should converge using increasingly finer resolution and more DOFs. This convergence has been observed for the mean strain, and for the maximum strain until the plastic effect becomes dominant. Beyond this regime, the solution becomes mesh-dependent leading to a softer material response with finer meshes. This behavior is typical for stress-strain relations with softening and indicates that regularization techniques are required in future to circumvent this pathological behavior; see [43,44]. In this regard, non local plasticity and gradient plasticity approaches can be used to overcome these mesh dependency. These models introduce a characteristic length scale that defines a distance in which neighboring points influence the local material response; see, for instance, Bertram and Forest [45], Eringen [46], Junker et al. [47], Liebe and Steinmann [48], Rosenbusch et al. [49].

To summarize, exploiting the potential of HPC resulted in highly resolved, coupled thermo-mechanical simulations of LBW processes with million degrees of freedom, distributed across thousands of parallel compute cores. A complete 2.4 s simulation of the CTW test was executed within hours on massively parallel architectures, showing a good qualitative agreement with experiments. A large part of the computing time is spent solving large linear systems of equation within the Newton solvers within the individual time steps. Here, as already mentioned, we use parallel domain decomposition methods. The HPC optimization of these preconditioned iterative linear solvers is the subject of [20]. Further optimizations in the future will concern the convergence of Newton's method itself. We are working on nonlinear domain decomposition methods and also on a more sophisticated control of the time step widths. For a quantitative prediction of solidification cracks, further steps must be taken, such as the consideration of the multiscale nature of this process. From a mechanical point of view, the implementation of a multiscale model in FE2TI is considered the next major task to take microscopic effects into account. With a modified $FE^2$ approach, micro and macro scales will be coupled and anisotropy due to the grain structure of the resolidified material can be implemented and analyzed. On the other hand, the experimental evaluation algorithms must be further improved, to minimize the accumulated error and provide a higher accuracy especially for strain computations based on the obtained displacement distribution. This must involve a further improvement of the image resolution as well as the application of different numerical filters.

## CRediT authorship contribution statement

**Tommaso Bevilacqua:** Writing – original draft, Visualization, Validation, Software, Investigation, Formal analysis, Data curation, Conceptualization; **Andrey Gumenyuk:** Writing – original draft, Visualization, Validation, Methodology, Investigation, Formal analysis; **Niloufar Habibi:** Writing – original draft, Visualization, Validation, Investigation, Formal analysis, Data curation; **Philipp Hartwig:** Visualization, Validation, Methodology, Investigation, Formal analysis, Data curation; **Axel Klawonn:** Writing – review & editing, Writing – original draft, Supervision, Methodology, Investigation, Funding acquisition, Conceptualization; **Martin Lanser:** Writing – review & editing, Writing – original draft, Validation, Supervision, Methodology, Investigation, Data curation, Conceptualization; **Michael Rethmeier:** Writing – review & editing, Supervision, Methodology, Investigation, Funding acquisition, Conceptualization; **Lisa Scheunemann:** Writing – review & editing, Writing – original draft, Supervision, Methodology, Investigation, Formal analysis, Conceptualization; **Jörg Schröder:** Writing – review & editing, Validation, Supervision, Methodology, Investigation, Funding acquisition, Formal analysis, Conceptualization.

## Data availability

Data is available on request but the code is confidential.

## Declaration of competing interests

Axel Klawonn reports financial support was provided by Deutsche Forschungsgemeinschaft. Martin Lanser reports financial support was provided by Deutsche Forschungsgemeinschaft. Joerg Schroeder reports financial support was provided by Deutsche Forschungsgemeinschaft. Lisa Scheunemann reports financial support was provided by Deutsche Forschungsgemeinschaft. Andrey Gumenyuk reports financial support was provided by Deutsche Forschungsgemeinschaft. Michael Rethmeier reports financial support was provided by Deutsche Forschungsgemeinschaft. If there are other authors, they declare that they have no known competing financial interests or personal relationships that could have appeared to influence the work reported in this paper.

## Acknowledgment

This research is funded by the Deutsche Forschungsgemeinschaft (DFG, German Research Foundation) - 434,946,896 within the research unit FOR 5134 "Solidification Cracks during Laser Beam Welding: High Performance Computing for High Performance Processing" and 465,316,565 within the research grant "Design and development of a measuring method to determine the strain state during hot crack initiation". The authors gratefully acknowledge the scientific support and HPC resources provided by the Erlangen National High Performance Computing Center (NHR@FAU) of the Friedrich-Alexander-Universität Erlangen-Nürnberg (FAU) under the NHR project k109be10. NHR funding is provided by federal and Bavarian state authorities. NHR@FAU hardware is partially funded by the German Research Foundation (DFG) - 440719683. Interchange and data storage was carried out by exploiting Kadi4Mat [50].

## References

[1] G. Agarwal, Study of Solidification Cracking During Laser Welding in Advanced High Strength Steels: A Combined Experimental and Numerical Approach, Ph.D. thesis, Delft University of Technology, 2019. https://doi.org/10.4233/UUID:DD0E5AB0-1427-4ECC-A8D8-4E8F35050FCA
[2] J.C. Lippold, Solidification behavior and cracking susceptibility of pulsed-laser welds in austenitic stainless steels, Welding J. (Miami);(United States) 73 (6) (1994)129–139.
[3] M. Norouzian, M.A. Elahi, P. Plapper, A review: suppression of the solidification cracks in the laser welding process by controlling the grain structure and chemical compositions, J. Adv. Joining Process. 7 (2023) 100139. https://doi.org/10.1016/j.jajp.2023.100139
[4] N. Prokhorov, Resistance to hot tearing of cast metals during solidification, Russ. Cast. Prod. 2 (2) (1962) 172–175.
[5] V. Quiroz, A. Gumenyuk, M. Rethmeier, Investigation of the hot cracking susceptibility of laser welds with the controlled tensile weldability test, J. Strain Anal. Eng. Design 47 (8) (2012) 587–599. https://doi.org/10.1177/0309324712462120
[6] N. Bakir, Development of Optical Measurement Technique to Determine the Critical Conditions for Solidification Cracking for Laser Welded Joints, Ph.D. thesis, Technische Universität Berlin, 2020.
[7] E. Friedman, Thermomechanical analysis of the welding process using the finite element method, J. Press. Vessel Technol. 97 (3) (1975) 206–213. https://doi.org/10.1115/1.3454296
[8] H.D. Hibbitt, P.V. Marcal, A numerical, thermo-mechanical model for the welding and subsequent loading of a fabricated structure, Comput. Struct. 3 (5) (1973) 1145–1174. https://doi.org/10.1016/0045-7949(73)90043-6
[9] O. Murua, J.I. Arrizubieta, A. Lamikiz, H.I. Schneider, Numerical simulation of a laser beam welding process: from a thermomechanical model to the experimental inspection and validation, Thermal Sci. Eng. Progress 55 (2024) 102901.
[10] Simufact Engineering (by Hexagon), Simufact additive (2025). [Software], https://www.hexagon.com/products/simufact-additive.
[11] S. Dinesh, J. Sahu, Thermomechanical simulation and experimental validation of distortion and residual stress for LPBF additive manufactured Inconel 718, Mater. Today Commun. 42 (2025) 111512.
[12] M. Jiménez-Xamán, M. Hernández-Hernández, R. Tariq, S. Landa-Damas, M. Rodríguez-Vázquez, A. Aranda-Arizmendi, P. Cruz-Alcantar, Numerical simulations and mathematical models in laser welding: a review based on physics and heat source models, Front. Mech. Eng. Volume 10 - 2024 (2024).
[13] N. Bakir, A. Gumenyuk, M. Rethmeier, Determination of critical local straining conditions for solidification cracking at laser beam welding by experimental and numerical methods, PAMM 24 (2) (2024) e202400020. https://doi.org/10.1002/pamm.202400020
[14] E. Ranjbarnodeh, Y.G. Anzabi, H. Sabet, Finite element modeling of the effect of welding parameters on solidification cracking of austenitic stainless steel 310, Metall. Mater. Eng. 22 (4) (2016) 237–250. https://doi.org/10.30544/222
[15] A. Klawonn, S. Köhler, M. Lanser, O. Rheinbach, Computational homogenization with million-way parallelism using domain decomposition methods, Comput. Mech. 65 (1) (2020) 1–22. https://doi.org/10.1007/s00466-019-01749-5
[16] S. Balay, S. Abhyankar, M.F. Adams, S. Benson, J. Brown, P. Brune, K. Buschelman, E. Constantinescu, L. Dalcin, A. Dener, V. Eijkhout, J. Faibussowitsch, W.D. Gropp, V. Hapla, T. Isaac, P. Jolivet, D. Karpeev, D. Kaushik, M.G. Knepley, F. Kong, S. Kruger, D.A. May, L.C. McInnes, R.T. Mills, L. Mitchell, T. Munson, J.E. Roman, K. Rupp, P. Sanan, J. Sarich, B.F. Smith, H. Suh, S. Zampini, H. Zhang, H. Zhang, J. Zhang, PETSc/TAO Users Manual, Technical Report ANL-21/39 - Revision 3.22, Argonne National Laboratory, 2024. https://doi.org/10.2172/2205494
[17] J.C. Simo, C. Miehe, Associative coupled thermoplasticity at finite strains: formulation, numerical analysis and implementation, Comput. Methods Appl. Mech. Eng. 98 (1) (1992) 41–104. https://doi.org/10.1016/0045-7825(92)90170-O

[18] R. von Mises, Mechanik der festen Körper im plastisch-deformablen Zustand, Nachr. Ges. Wiss. Göttingen, Math.-Phys. Kl. 1913 (1913) 582–592. http://eudml.org/doc/58894.

[19] J.C. Simo, R.L. Taylor, K.S. Pister, Variational and projection methods for the volume constraint in finite deformation elasto-plasticity, Comput. Methods Appl. Mech. Eng. 51 (1–3) (1985) 177–208. https://doi.org/10.1016/0045-7825(85)90033-7

[20] T. Bevilacqua, A. Klawonn, M. Lanser, Highly scalable two-level monolithic overlapping Schwarz preconditioners for thermo-elastoplastic laser beam welding problems, Comput. Mech. (2025). https://doi.org/10.1007/s00466-025-02674-6

[21] T. Bevilacqua, A. Klawonn, M. Lanser, A. Wasiak, Monolithic overlapping Schwarz preconditioners for nonlinear finite element simulations of laser beam welding processes, in: F. Marmo, S. Cuomo, A. Cutolo (Eds.), Computational Mechanics and Applied Mathematics: Perspectives from Young Scholars, Springer Nature Switzerland, Cham, 2025, pp. 123–133. https://doi.org/10.1007/978-3-031-76591-9

[22] A. Toselli, O. Widlund, Domain Decomposition Methods-Algorithms and Theory, 34 of *Springer series in computational mathematic*, Springer Berlin, Heidelberg, Berlin, Berlin, 2006.

[23] C.R. Dohrmann, A. Klawonn, O.B. Widlund, Domain decomposition for less regular subdomains: overlapping Schwarz in two dimensions, SIAM J. Numer. Anal. 46 (4) (2008) 2153–2168. https://doi.org/10.1137/070685841

[24] C.R. Dohrmann, A. Klawonn, O.B. Widlund, A family of energy minimizing coarse spaces for overlapping Schwarz preconditioners, in: Domain Decomposition Methods in Science and Engineering XVII, 60, Springer Berlin Heidelberg, Berlin, Heidelberg, 2008, pp. 247–254. https://doi.org/10.1007/978-3-540-75199-1

[25] A. Heinlein, C. Hochmuth, A. Klawonn, Monolithic overlapping Schwarz domain decomposition methods with GDSW coarse spaces for incompressible fluid flow problems, SIAM J. Sci. Comput. 41 (4) (2019) C291–C316. https://doi.org/10.1137/18M1184047

[26] T. Lienert, J. Lippold, Improved weldability diagram for pulsed laser welded austenitic stainless steels, Sci. Technol. Weld. Joining 8 (1) (2003) 1–9. https://doi.org/10.1179/136217103225008847

[27] N. Coniglio, Aluminum Alloy Weldability: Identification of Weld Solidification Cracking Mechanisms Through Novel Experimental Technique and Model Development, Ph.D. thesis, Technische Universität Berlin, Berlin, 2008.

[28] A. Gumenyuk, N. Bakir, M. Rethmeier, Two-colour thermography for measurement of temperature distribution in laser beam welding, Procedia CIRP 124 (2024) 468–471. https://doi.org/10.1016/j.procir.2024.08.155

[29] N. Bakir, V. Pavlov, S. Zavjalov, S. Volvenko, A. Gumenyuk, M. Rethmeier, Development of a novel optical measurement technique to investigate the hot cracking susceptibility during laser beam welding, Welding World 63 (2019) 435–441. https://doi.org/10.1007/s40194-018-0665-8

[30] R.L. Taylor, FEAP - Finite element analysis program, version 8.2, 2008. http://www.ce.berkeley/feap.

[31] J.C. Simo, T.J.R. Hughes, Computational Inelasticity, number v. 7 in Interdisciplinary applied mathematics, Springer, New York, New York, 1998.

[32] A. Artinov, M. Bachmann, M. Rethmeier, Equivalent heat source approach in a 3D transient heat transfer simulation of full-penetration high power laser beam welding of thick metal plates, Int. J. Heat Mass Transf. 122 (2018) 1003–1013. https://doi.org/https://doi.org/10.1016/j.ijheatmasstransfer.2018.02.058

[33] A. Artinov, V. Karkhin, N. Bakir, X. Meng, M. Bachmann, A. Gumenyuk, M. Rethmeier, Lamé curve approximation for the assessment of the 3D temperature distribution in keyhole mode welding processes, J. Laser Appl. 32 (2) (2020) 022042. https://doi.org/10.2351/7.0000076

[34] E. Group, Sysweld material database, 2009, (Software), https://www.esi-group.com/products/sysweld.

[35] H. Hu, S.A. Argyropoulos, Mathematical modelling of solidification and melting: a review, Modell. Simul. Mater. Sci. Eng. 4 (4) (1996) 371. https://doi.org/10.1088/0965-0393/4/4/004

[36] Y. Qin, Y. Bao, S. DeWitt, B. Radhakrishnan, G. Biros, Dendrite-resolved, full-melt-pool phase-field simulations to reveal non-steady-state effects and to test an approximate model, Comput. Mater. Sci 207 (2022) 111262. https://doi.org/https://doi.org/10.1016/j.commatsci.2022.111262

[37] F. Richter, Die physikalischen Eigenschaften der Stähle: das 100-Stähle-Programm, Arbeitskreis Thermophysik GEFTA: Berlin, Germany (2010).

[38] R. Chandra, Parallel Programming in OpenMP, Morgan Kaufmann, San Francisco, CA, United States, San Francisco, CA, United States, 2001. https://doi.org/10.5555/355074

[39] A. Klawonn, M. Lanser, O. Rheinbach, M. Uran, Fully-coupled micro-macro finite element simulations of the Nakajima test using parallel computational homogenization, Comput. Mech. 68 (5) (2021) 1153–1178. https://doi.org/10.1007/s00466-021-02063-9. https://doi.org/10.1007/s00466-021-02063-9

[40] Intel Corporation, Intel® oneAPI Math Kernel Library PARDISO, 2024. Accessed: January 17, 2025, https://www.intel.com/content/www/us/en/docs/onemkl/developer-reference-c/2024-0/onemkl-pardiso-parallel-direct-sparse-solver-iface.html.

[41] O. Schenk, K. Gärtner, W. Fichtner, A. Stricker, PARDISO: a high-performance serial and parallel sparse linear solver in semiconductor device simulation, Future Gener. Comput. Syst. 18 (1) (2001) 69–78. https://doi.org/10.1016/S0167-739X(00)00076-5

[42] C. Miehe, A theory of large-strain isotropic thermoplasticity based on metric transformation tensors, Arch. Appl. Mech. 66 (1995) 45–64. https://doi.org/10.1007/BF00786688

[43] P. Wriggers, Nonlinear finite element methods, Springer Science & Business Media, 2008.

[44] S. Wu, X. Wang, Mesh dependence and nonlocal regularization of one-dimensional strain softening plasticity, J. Eng. Mech. 136 (11) (2010) 1354–1365.

[45] A. Bertram, S. Forest, The thermodynamics of gradient elastoplasticity, Continuum Mech. Thermodyn. 26 (3) (2014) 269–286.

[46] A.C. Eringen, On nonlocal plasticity, Int. J. Eng. Sci. 19 (12) (1981) 1461–1474. https://doi.org/https://doi.org/10.1016/0020-7225(81)90072-0

[47] P. Junker, J. Riesselmann, D. Balzani, Efficient and robust numerical treatment of a gradient-enhanced damage model at large deformations, Int. J. Numer. Methods Eng. 123 (3) (2022) 774–793.

[48] T. Liebe, P. Steinmann, Theory and numerics of a thermodynamically consistent framework for geometrically linear gradient plasticity, Int. J. Numer. Methods Eng. 51 (12) (2001) 1437–1467.

[49] S.M. Rosenbusch, D. Balzani, J.F. Unger, Regularization of softening plasticity models for explicit dynamics using a gradient-enhanced modified Johnson-Holmquist model, Int. J. Impact Eng. 198 (2025) 105209. https://doi.org/https://doi.org/10.1016/j.ijimpeng.2024.105209

[50] N. Brandt, L. Griem, C. Herrmann, E. Schoof, G. Tosato, Y. Zhao, P. Zschumme, M. Selzer, Kadi4Mat: a research data infrastructure for materials science, Data Sci. J. 20 (2021) 8. https://doi.org/10.5334/dsj-2021-008